

Alistair A. Young, PhD • Leon Axel, PhD, MD • Lawrence Dougherty, MSE
Daniel K. Bogen, PhD, MD • Chantal S. Parenteau, MSE

Validation of Tagging with MR Imaging to Estimate Material Deformation¹

Myocardial tagging with magnetic resonance imaging is useful for non-invasive estimation of in vivo heart wall deformation. To validate the method of strain estimation and quantify the error of deformation estimates, a deformable silicone gel phantom in the shape of a cylindrical anulus was built and imaged. Four observers digitized the displacement of magnetic tags in two deformation modes: axial shear, caused by a 45° rotation of the inner cylinder, and azimuthal shear, caused by a 13.5-mm longitudinal translation of the inner cylinder. In axial shear, good agreement was found between the angular displacement of stripes painted on the gel and an analytic solution. Displacement of magnetic tags also agreed with that solution. Interobserver and observer-model errors in deformation estimates were quantified for homogeneous and nonhomogeneous strain analysis. In homogeneous strain analysis, errors in point localization produced relatively large errors, which were reduced in nonhomogeneous strain analysis. Both estimates were unbiased across the range of deformations.

Index terms: Heart, function, 51.121412 • Magnetic resonance (MR), experimental • Magnetic resonance (MR), physics • Magnetic resonance (MR), pulse sequences • Phantoms

Radiology 1993; 188:101-108

¹ From the Department of Radiology, Hospital of the University of Pennsylvania, 308 Stemmler Hall, 36th St and Hamilton Walk, Philadelphia, PA 19104-6086 (A.A.Y., L.A., L.D.); and Department of Bioengineering, University of Pennsylvania, Philadelphia (D.K.B., C.S.P.). Received October 28, 1992; revision requested December 10; revision received January 22, 1993; accepted February 16. Supported in part by National Institutes of Health grant HL-43014 of the National Heart, Lung, and Blood Institute. Address reprint requests to L.A.

[†] RSNA, 1993

ACCURATE estimates of heart wall motion and deformation are necessary to evaluate normal and abnormal contraction and to model cardiac mechanics (1,2). Myocardial tissue tagging with magnetic resonance (MR) imaging has enabled noninvasive measurement of material displacement (3,4) and deformation (5,6) in both normal and diseased hearts (7,8). With spatial modulation of magnetization (SPAMM), two orthogonal sets of magnetic saturation planes, each orthogonal to the image plane, can be created in a short interval (9). The stripes persist for times on the order of the longitudinal relaxation time T1 and often can be tracked throughout systole. The intersections of the stripes with each other and the image plane provide two-dimensional information about the displacement of material points. The relative motions of markers have been analyzed to calculate local strain and rotation with methods previously used in implanted radiopaque beads and ultrasonic crystals (10,11). If one assumes a constant state of strain (homogeneous strain [HS]) within a small group of markers (three to six points) at each deformed state, it is possible to calculate the deformation gradient tensor (eg, with linear least-squares fitting [5,10,12,13]). Alternatively, higher-order finite elements may be fitted to the motion of more markers (typically 10-15 markers) and may thereby enable nonhomogeneous strain calculation and some immunity to digitization noise (14,15).

Validation of these techniques is made difficult by the absence of a reliable standard against which to compare methods for wall-motion measurement. The most confidence has been placed in implanted markers (16); however, comparison between markers and tagged MR images is difficult. One study (17) compared circumferential shortening in SPAMM images with implanted ultrasonic

crystals and found greater shortening in normal tissue with the SPAMM technique than with the crystals. This difference in shortening may have been due to damage caused by crystal implantation, together with the difficulty in location of tags between crystals due to susceptibility artifacts. Other validation of MR tagging has involved the use of rigid rotating phantoms, which demonstrate that these motions are accurately reproduced (18). However, validation of MR tagging as a method for measurement of deformation and strain requires a deformable phantom with known or independently measured deformations. Such a phantom must satisfy the following criteria:

1. The material should have magnetic properties (T1 and T2) similar to those of heart wall tissue and produce a good signal-to-noise ratio (S/N) in a conventional MR imager.
2. The material should be able to undergo large elastic deformations (20% or greater) in a cyclic manner with period on the order of T1. In conventional spin-echo (SE) MR imaging, at least 128 excitations (deformation cycles) are required to generate an MR image of adequate resolution.
3. The phantom should enable an independent method for displacement measurement, such as optical tracking of points.
4. Finally, it would be desirable to calculate the deformation with a mathematical model and thereby enable comparison of exact (calculated) and measured displacement and strain fields. Such a model should be

Abbreviations: E = Lagrangian strain tensor, F = deformation strain tensor, HS = homogeneous strain, R = rotation tensor, RMS = root mean square, SE = spin echo, S/N = signal-to-noise ratio, SPAMM = spatial modulation of magnetization, U = right stretch tensor.

based on the theory of finite elasticity and should be based on a realistic material law (stress and strain relation).

To validate the method of strain estimation with MR tagging and quantify the errors involved, we designed and built a deformable silicone gel phantom that enables controlled deformations. A similar silicone gel system (model Q7-2218; Dow Corning, Midland, Mich) has been suggested for use in MR imaging (19) because it has T1 and T2 values within the range of human tissue and can be cast into a variety of shapes. In addition, the elastic properties of the gel can be adjusted to resemble a range of biologic tissues, and it has been used to model the response of brain tissue to large rotational accelerations (20). The gel system is composed of two parts, catalyst (part A) and resin (part B), the ratio of which determines its elastic properties. (A decrease in A:B produces stiffer gels.) The MR signal is derived entirely from methyl protons; the dependence of T1 and T2 on A:B is examined in reference 19. We used the industrial counterpart of model Q7-2218 (Sylgard Primerless Dielectric Gel 527; Dow Corning). This gel has similar properties to Q7-2218 but is industrial rather than medical grade.

A cylindrical annulus geometry was chosen because analytic solutions exist for constrained deformations of this geometry (21–23). For simplicity, only axisymmetric shearing deformations were permitted. In these cases, imaging planes were chosen in which the motion was in-plane (no motion through the imaging plane). This enabled direct comparison of the two-dimensional displacement of magnetic tags in the image with the true motion. Radial stripes were painted onto the surface of the gel and tracked with the help of a video camera and digitizer. Analytic solutions for the deformation were readily obtained on assumption of a simple law of rubberlike material known as the Mooney-Rivlin strain energy function (21,23). The mathematical model was verified by comparison with the optically measured deformation of the painted stripes. In turn, the magnetic tagging technique was verified by comparison with the analytic solution. The mathematical model enabled the quantification of errors in strain estimation due to both the approximation of HS within marker triangles and the effect of interobserver variation in tag location. Finally, a higher-order finite element analysis

was performed on the same data to ascertain the degree of improvement possible with this technique for non-homogeneous estimation of strain.

MATERIALS AND METHODS

Phantom Construction

The geometry of the deformable phantom consisted of two concentric Delrin cylinders (inner and outer [Fig 1]) attached to two Lucite end plates. The inner cylinder penetrated the two end plates through Teflon bearings. Parts A and B of the gel system were mixed in a 1:1 ratio, stirred for 5 minutes, poured into the cavity between the inner and outer cylinders, and allowed to cure for 5 days. A 1:1 ratio was chosen for the cylindrical phantom because it provided a good combination of flexibility under shear and integrity of shape under inertial forces (including gravity). The bottom end plate, which had been greased with Vaseline jelly before casting, was then separated from the gel and reattached to the outer cylinder by means of spacing washers. Thus, the gel was firmly attached by its own adhesion to the inner and outer surfaces of the cylinder, with end surfaces free. The inner cylinder was constrained to either (a) rotate or (b) longitudinally translate with regard to the outer cylinder, thereby producing axial transverse shear or azimuthal transverse shear, respectively, within the gel. The inner cylinder was rotated by pulling a lever arm attached to the axle (Fig 1). Two stops were positioned on the front end plate to limit the arc of travel of the lever arm to 45°. Adjustable Teflon washers attached to the axle limited the longitudinal translation of the inner cylinder to a range of 0–15 mm. The dimensions of the gel phantom were as follows: inner radius, 19.0 mm; outer radius, 47.6 mm; and length, 35 mm.

In each method of deformation estimation (optical, MR imaging, and analytic), motion was represented by means of a cylindrical polar coordinate system in which a material point initially at (R, Θ, Z) in the undeformed state moves to (r, θ, z) in the deformed state. This system was aligned with the phantom so that the undeformed gel occupied the region $0 \leq Z \leq 35$ and $R_1 \leq R \leq R_2$, with $R_1 = 19.0$ and $R_2 = 47.6$.

Optical Measurement

In the case of axial shear, angular displacement can be expressed as a function of undeformed radius: $\omega(R)$. The components of displacement in the radial and longitudinal directions were very small relative to the angular component and therefore were ignored. To evaluate the angular displacement function, four lines (1 mm thick each) were painted onto one of the free end surfaces of the gel in radial orientations (ie, constant θ lines). This end was viewed with a video camera, and images of the undeformed and deformed

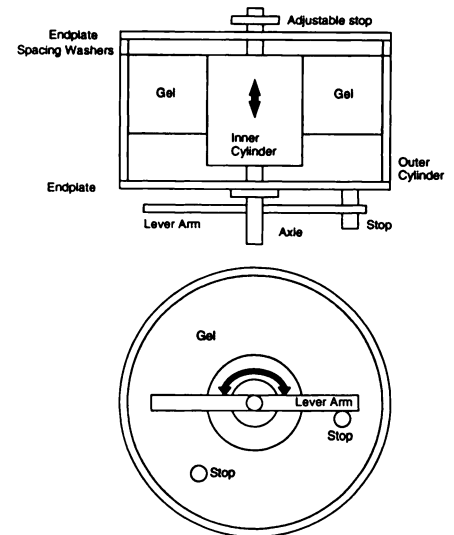


Figure 1. Schema of phantom construction. Plan (top) and elevation (bottom) show directions of motion (double arrows).

states were digitized with a video frame grabber. The digitized coordinates were scaled with a 1-cm grid imaged in the same location and then were converted to cylindrical polar coordinates. Each line was sampled at 10 points approximately equally spaced along its length in the undeformed state. Corresponding points in the deformed state were found along the same line with the same radial coordinate as that of the undeformed points. The angular displacement between corresponding points was then calculated and plotted as a function of radius.

Measurement with MR Imaging

The phantom was secured firmly in a transmit-receive extremity coil 17 cm in diameter and imaged with a 1.5-T superconducting magnet (Signa; GE Medical Systems, Milwaukee, Wis). Images were obtained in the central circumferential plane of the phantom (constant Z) in the case of axial shear and in a central longitudinal plane (constant θ) in the case of azimuthal shear. In both cases, symmetry of both the phantom geometry and the displacement boundary conditions imply that no through-plane motion can be present. The SPAMM pulse sequence (9) was used to generate an orthogonal tagging grid with an interstripe spacing of 5 mm and stripe width of approximately 1 mm in 12 msec. After tagging, there was a delay of 700 msec while the phantom was manipulated into its deformed position. A conventional SE MR imaging pulse sequence was then performed, followed by a further delay of 700 msec before the cycle repeated. Images in the undeformed position were also obtained without motion. Thus, only stop-to-stop motion was imaged. A 3-mm section thickness was used, and 128 phase encodings (each of which required a deformation cycle) were obtained with a 20-cm field of view. The image was reconstructed to a 256×256 ma-

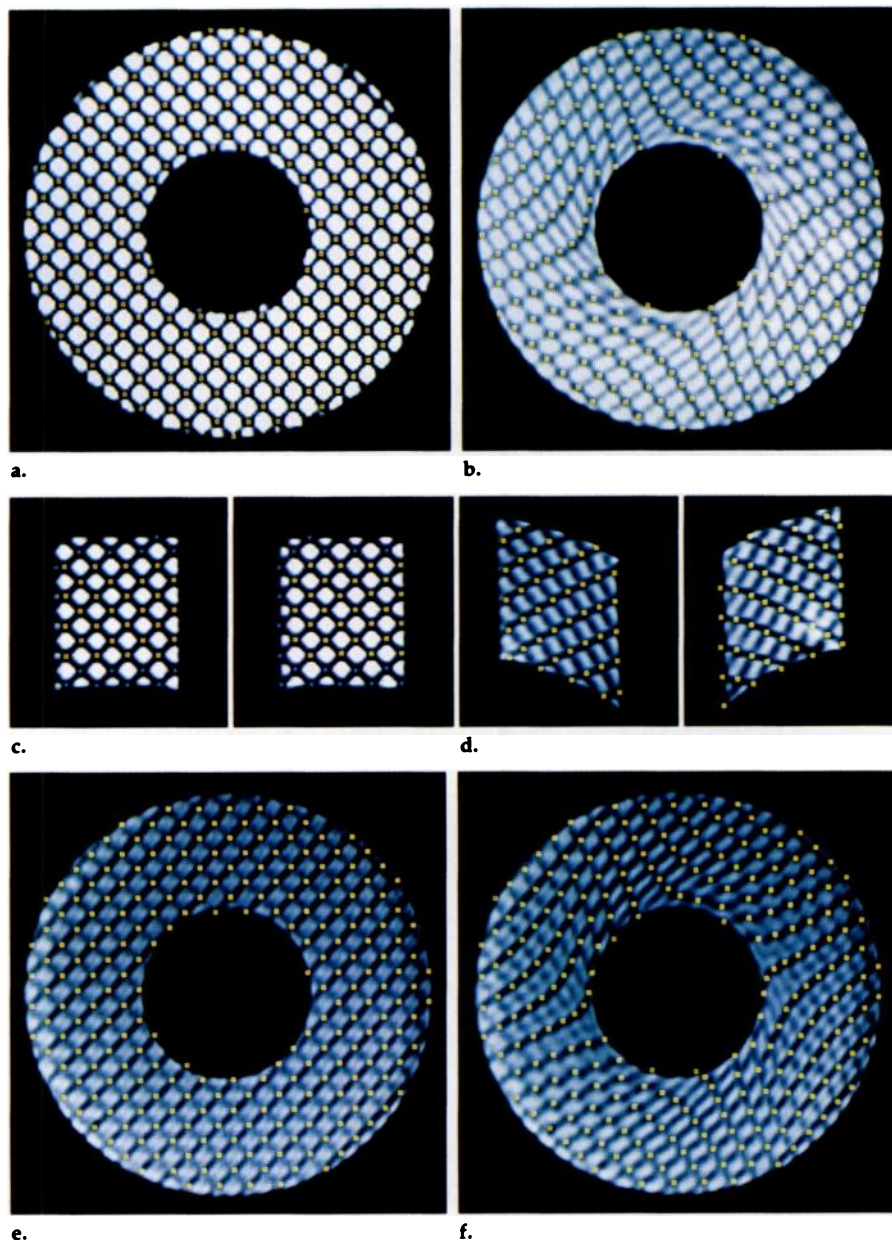


Figure 2. SPAMM images. Yellow squares denote position of tag intersections predicted by means of the analytic solution. (a) Axial shear undeformed. (b) Axial shear deformed. (c) Azimuthal shear undeformed. (Blue points are not used in the analysis.) (d) Azimuthal shear deformed. (e) Single-shot axial shear undeformed. (f) Single-shot axial shear deformed.

trix with a pixel size of 0.78 mm (Fig 2). A tag flip angle of 180° and an echo time (TE) of 27 msec were used with a net repetition time of approximately 1,500 msec. In subsequent experiments, a single-shot gradient-recalled-echo (GRE) imaging technique was used in which the entire image could be acquired with a single SPAMM excitation (one deformation cycle). This technique used a spoiled GRE in the steady state pulse sequence with a 256×128 sampling of k space by means of a simple linear ramp in the phase-encoding direction (24,25). Two circumferential planes were acquired in axial shear mode, one at the edge and one in the center ($Z = 2.5$ and $Z = 17.5$ mm), each with four signals averaged (four deformation cycles). For both axial and azimuthal shear, deforma-

tion was produced manually by means of nylon cables attached to the inner cylinder and lever arm (pull-pull actuation). Figure 2 shows the deformed and undeformed images obtained with both conventional SE MR and single-shot GRE imaging techniques. The ratio of contrast (difference between striped and unstriped regions) to noise (C/N) (standard deviation) in the deformed images was approximately 4.5, similar to that in end-systole images of the human heart (C/N, 3.5–4.5).

The MR images were transferred to a custom-written analysis package (5). The center of the phantom was chosen by manually fitting a circle of correct diameter to the contour of the inner cylinder. (A rectangle was used in the azimuthal shear.) Tag intersection points were man-

ually determined on a zoomed interpolated image (magnification, $\times 5$) and tracked between undeformed and deformed states. Image coordinates were converted to cylindrical polar coordinates for comparison of displacement and deformation. Each image was analyzed independently by four observers.

Homogeneous Analysis of Deformation

Deformation can be measured in a variety of ways. A useful measure in cases of large displacements is the Lagrangian strain tensor E , which relates a small line segment dX of length ds in the undeformed state to its deformed state dx of length ds (23): $ds^2 - dS^2 = 2dX^T E dX$. The deformation gradient tensor F relates the deformed and undeformed line segments: $dx = F dX$. Triangles of adjacent markers were selected to calculate deformation, with the HS approximation within the triangle. The deformation gradient tensor F was calculated from the relative displacements of the vertices (5,12,13). This was then used to calculate E :

$$E = \frac{1}{2} (F^T F - I), \quad (1)$$

and the associated rotation tensor R and right stretch tensor U :

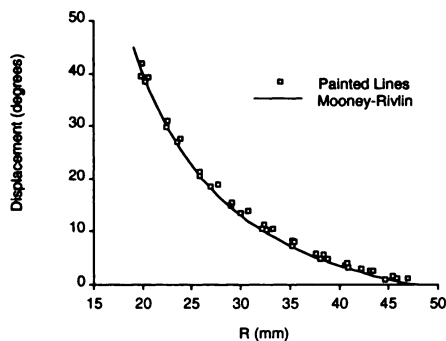
$$F = RU \quad (2)$$

The principal strains were considered to be the eigenvalues of E (λ_1 and λ_2 , with $\lambda_1 \geq \lambda_2$), which are the most positive and most negative strains experienced by the gel at that point. The principal direction β was defined as the angle between the eigenvector associated with λ_1 and the radial direction. The angle of rotation α was calculated from the rotation tensor R (5), giving the rigid body rotation of the triangle. Finally, the relative change in area of the triangle, ΔA , was calculated from the product of the eigenvalues of U .

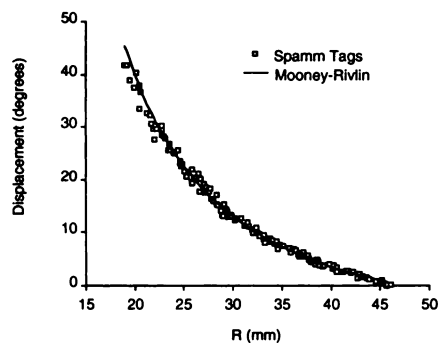
Wherever possible, the triangles were oriented with the longest side perpendicular to the radial coordinate to maximize the number of triangles across the wall (the direction in which the deformation was changing).

Nonhomogeneous Analysis of Deformation

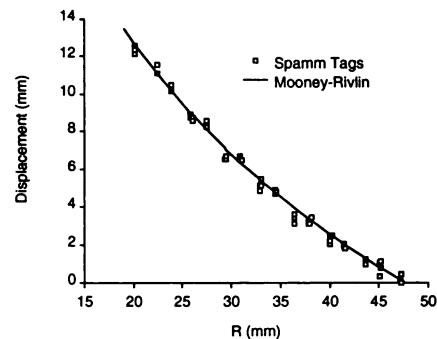
The motions of the magnetic tag intersections were also analyzed with a finite-element model of the deformation. The method was a two-dimensional version of that used to estimate nonhomogeneous strain distributions from bifurcations of the coronary arteries (14) and arrays of radiopaque implanted markers (15). In the case of axial shear, four bicubic Hermite elements were used to describe the central Z plane of the anulus, with nodes equally spaced in the angular direction at 90° increments. These elements were specified in rectangular Cartesian coordinates with element coordinates that were initially aligned in radial and circumferential di-



3.



4.



5.

Figures 3–5. (3) Angular displacements for axial shear; optical measurement of painted lines is compared with analytic solution obtained by means of the Mooney-Rivlin strain energy function (*Mooney-Rivlin* in 3–5). In 3–5, R = radial position. (4) Angular displacements for axial shear; magnetic tags are compared with analytic solution. In 4 and 5, *Spamm* = SPAMM. (5) Longitudinal displacements for azimuthal shear; magnetic (*Spamm*) tags are compared with analytic solution.

rections. In the case of azimuthal shear, a single bicubic element was used to model the right side of the gel image, with element coordinates initially aligned in the radial and longitudinal directions.

After the element coordinates of the tag intersections were calculated, the mesh was deformed to fit the displaced locations of the tag intersections by means of the linear least-squares method (14,15). Comparison between the two states (undeformed and deformed) enables calculation of the nonhomogeneous deformation gradient tensor—and hence the quantities λ_1 , λ_2 , β , α , and ΔA —at any material (element) point within the finite-element model.

Mathematical Model

On assumption of a simple, isotropic, incompressible-material law for the gel, analytic solutions were obtained for both deformation modes (Appendix). The nonhomogeneous deformation gradient tensor can be calculated analytically from the displacement field (Appendix), without the need to construct elements. E , R , and U were calculated with Equations (1) and (2), and the quantities λ_1 , λ_2 , β , α , and ΔA were calculated for the desired values of undeformed radius.

RESULTS

MR Imaging

A summary of the MR imaging properties of three samples with varying stiffness (part A:part B) is shown in Table 1. It can be seen that over the range tested the signal is proportional to the amount of part A in the mixture but that both T1 and T2 are relatively constant and are similar to values found in biologic tissue. Figure 2 shows both SE MR and single-shot GRE images. In some places, the deformed SPAMM stripes appear jagged or broken. This is due to undersampling in the phase-encoding direction and can be reduced by increasing the number of phase-encoding steps in

higher frequencies. In the axial shear images, the root mean square (RMS) error in tag intersection location between the four observers averaged 0.30 mm in the undeformed state and 0.42 mm in the deformed state. For azimuthal shear, these values were 0.19 and 0.29 mm.

Angular Displacement

The angular displacement of the painted stripes as a function of radius is plotted in Figure 3 in the case of axial shear caused by a 45° rotation of the inner cylinder. Comparison is made with the analytic model (Appendix). No appreciable deformation due to gravity or time-dependent behavior occurred after actuation of the deformation, a finding that implies that viscoelastic effects are small throughout the experiment. The RMS error between the measured and theoretically calculated angular displacements at the same radius was 1.01° ($n = 40$ points distributed over the undeformed radius, 10 in each stripe). In comparison, the RMS error in the angular coordinate of the undeformed stripes was 0.34° averaged over all points. Figure 3 shows that the model approximates the displacement field very well; the slight positive bias may be attributed to a small rigid body rotation of the entire phantom.

Figure 4 compares the angular displacement of the magnetic tags located by one observer with that of the model; like Figure 3, it shows good agreement between these displacements (RMS error, 0.80°; $n = 236$ points averaged over four observers). In the single-shot SPAMM images obtained at two circumferential planes (one at the free edge of the gel and one at the central plane of the gel), no appreciable difference in tag displacement from the SE central-plane image

Table 1
Magnetic Properties of Gel

A:B	Signal*	T1 (msec)	T2 (msec)
1:1	1,381	930	70
1:2	911	952	71
1:3	679	907	72

Note.—A:B = part A: part B.
*Arbitrary units.

was seen. This implies that nonangular displacements due to the Kelvin effect (Appendix) at the edges of the phantom are small for this deformation.

In the case of azimuthal shear caused by a 13.5-mm longitudinal translation of the inner cylinder (Fig 5), the RMS error in longitudinal translation between magnetic tags and the analytic model was 0.24 mm ($n = 56$ points averaged over four observers). Near the free edges of the gel, the deformed model did not fit the imaged intersections as well as in the interior region. This was due to a small radial displacement of the gel near the free edges that was ignored in the analytic model. Thus, for the case of azimuthal shear, only the inner two-thirds of the phantom was used for error analysis.

Homogeneous Analysis of Deformation

Two sources of error exist in calculation of deformation from the relative motions of triangle vertices: The first source—inaccuracy in selection of the intersection location on the image—is due to digitization, image S/N, image resolution, and human variability. The second source is the HS approximation within the triangle

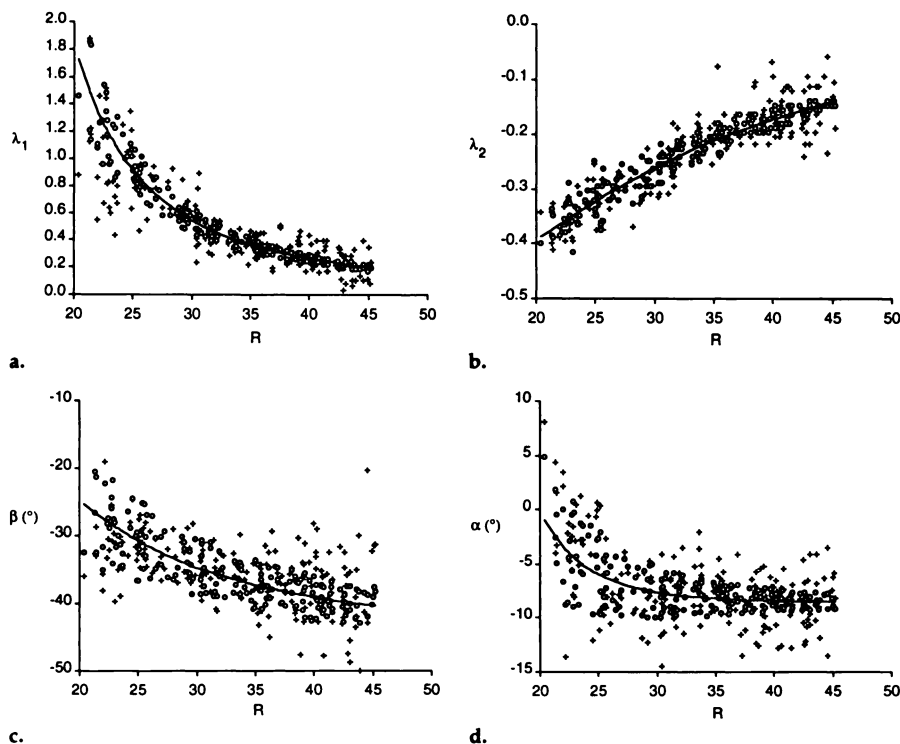


Figure 6. Contribution of error in point placement and HS approximation to deformation parameters. The curved line indicates the analytic solution. + = findings by one observer, O = modeled displacement (without noise) with the same HS analysis of triangles deformed according to the Mooney-Rivlin model. (a) Most positive eigenvalue. In a–d, numbers on x axis are millimeters; R = radial position. (b) Most negative eigenvalue. (c) Principal angle. (d) Rotation angle.

Table 2
Average Errors in Homogeneous Strain Calculation in Axial Shear

Comparison of Values	Average Error				
	λ_1	λ_2	β^*	α^*	ΔA
O/O	0.173	0.057	8.83	3.67	0.133
O/A	0.156	0.046	6.32	3.21	0.118
SSS/A	0.122	0.036	5.27	2.56	0.101
M/A	0.081	0.019	1.03	1.59	0.072
Percentage of analytic solution					
O/A	33	24	17	51	12
M/A	10	8	3	43	7

Note.—O/O = observer/observer, O/A = observers/analytic model, SSA/A = single-shot SPAMM image/analytic model, M/A = modeled displacement (noiseless)/analytic model, λ_1 and λ_2 = principal strains, β = principal angle, α = rotation angle, ΔA = change in area.

* Degrees, except for percentage of analytic solution.

(13). Figure 6 shows the deformation measured at the centroids of the marker triangles for the axial shear mode by one observer compared with the analytic solution. Also plotted in Figure 6 are the values obtained from an HS analysis of triangles deformed according to the Mooney-Rivlin model; these values show the error due to the HS approximation in the presence of perfect (noise-free) data. In most cases, it can be seen that the effect of noise in the data is to increase the HS error substantially. Table 2 summarizes the average interobserver and

observer-analytic model errors for HS calculation in axial shear. The observer-analytic model error (33% for λ_1 , 24% for λ_2) is approximately three times the expected noise-free estimate (modeled displacement/analytic model: 10% for λ_1 , 8% for λ_2). The percent error in rotation angle (α) is inflated because α approaches zero toward the inner cylinder (Fig 6d). Values based on the central-plane, single-shot SPAMM image were similar to values based on the conventional SE MR image, a finding that indicates that substantial errors are not intro-

duced with this method. Errors calculated for the azimuthal shear mode are presented in Table 3. All the estimates were unbiased (ie, the average error was not statistically significantly different from zero), the worst case being λ_1 in axial shear (average error, -0.009), which was underestimated by the observers in the inner 5 mm of radius.

Nonhomogeneous Analysis of Deformation

Bicubic Hermite, rectangular Cartesian elements were fitted to the measured displacements of the tag intersections recorded by each observer. The average RMS error between the tag locations in the deformed state and the locations predicted with the finite-element model was 0.35 mm for axial shear and 0.13 mm for azimuthal shear. These were both less than the interobserver error in point location in the deformed state (0.42 and 0.29 mm). Measurements of principal strains recorded by one observer are compared with the analytic solution in Figure 7. Table 4 summarizes the errors obtained between the nonhomogeneous strain calculated at each triangle centroid within the finite element model and the analytic solution. Azimuthal shear results are presented in Table 5.

DISCUSSION

Previous attempts to validate MR tagging as a method for strain estimation and to quantify the errors involved include comparisons between tags and ultrasonic crystals (17) and measurement of rigid body rotation (18). Direct in vivo comparison between tags and markers has been elusive because it is difficult to locate both tags and markers in the same region of tissue. Alternatively, experiments with rigid phantoms do not address the measurement of deformation.

We have designed a deformable silicone gel phantom that allows well-controlled axisymmetric deformations only. The deformation was repeatedly reproduced with stops to limit the travel of the lever arm and axle. Stop-to-stop deformation was analyzed with optical markers, magnetic tags, and a mathematical model. The displacements of the magnetic tags showed excellent agreement with both optical markers and the analytic solution. If the interobserver errors were independent and the mathemat-

ical model were exactly correct, we would expect the error between observers to be greater than the observer-model error by a factor of $\sqrt{2}$. In our study, they were approximately the same (cf O/O with O/A in Tables 2 and 3), a finding that indicates the existence of a small systematic component in the error between observers. This systematic component may be caused by a variety of factors: consistent human error (in axial shear near the inner cylinder, the observers tended to underestimate the displacement), systematic contributions due to field inhomogeneity, or violations of the assumptions that underlie the analytic model. However, the systematic component is small compared with the random error in point placement, because the error between observers is similar to the observer-model error. The errors obtained with single-shot SPAMM imaging were also similar to those obtained with conventional SE MR imaging, despite the increased sensitivity of the former to field inhomogeneities. GRE techniques are potentially very useful for reduction of respiration artifact in breath-hold images. Single-shot SPAMM images are also potentially important for examinations in which cyclic deformations are impossible (eg, in soft-tissue injury or musculoskeletal structures).

Homogeneous strain analysis of triangles yielded unbiased estimates of principal strains, principal angle, and rotation angle. However, noise in tag point location greatly increased error in point estimates over the noise-free case (Table 2). This error is largely due to the resolution of the images and is governed by the magnitude of the imaging magnetic field gradients. In addition, the spacing of the tags must be small compared with the gradient of the underlying strain field. A higher-order finite-element analysis reduced both the interobserver and observer-analytic solution errors (Table 4). The finite-element analysis enables some smoothing of the displacement field because, in general, there are fewer degrees of freedom in the mesh (nodal parameters) than data points. Furthermore, the strain may vary according to the order of the interpolation functions. Care must be taken that the finite-element model does not smooth out real variations in the data; a good check is the error between data points and their predicted locations in the deformed state, which should be on the order of the interobserver error in point location.

Table 3
Average Errors in Homogeneous Strain Calculation in Azimuthal Shear

Comparison of Values	RMS Error				
	λ_1	λ_2	β^*	α^*	ΔA
O/O	0.063	0.040	5.59	2.09	0.075
O/A	0.075	0.031	5.31	2.10	0.062
M/A	0.010	0.003	0.15	0.29	0.011
Percentage of analytic solution					
O/A	24	17	10	15	6
M/A	3	3	1	2	1

Note.—O/O = observer/observer, O/A = observers/analytic model, M/A = modeled displacement (noiseless)/analytic model, λ_1 and λ_2 = principal strains, β = principal angle, α = rotation angle, ΔA = change in area.

* Degrees, except for percentage of analytic solution.

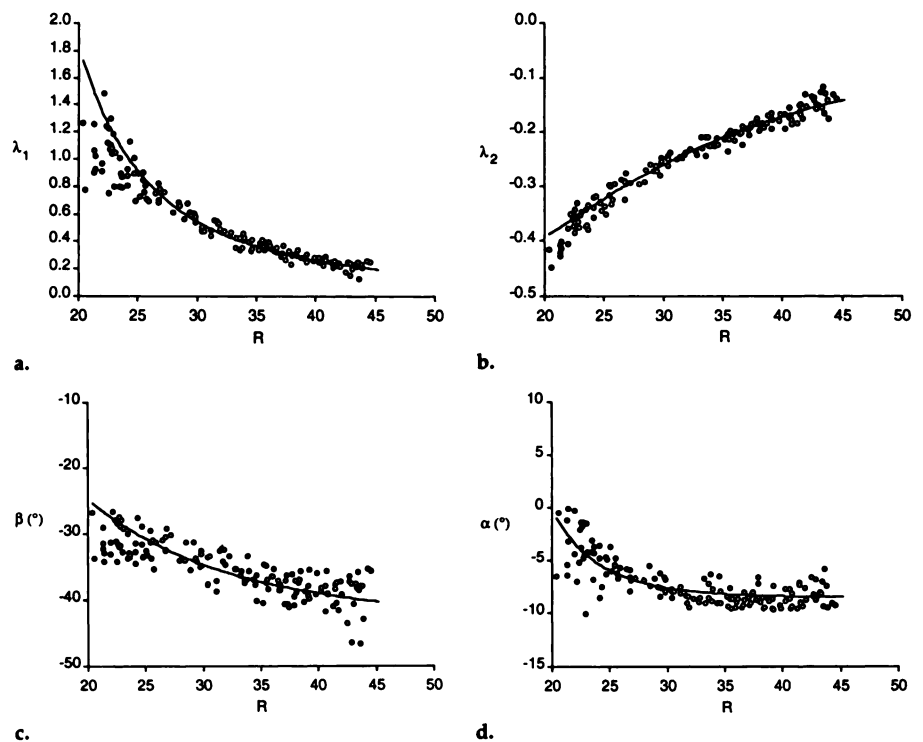


Figure 7. Comparison of nonhomogeneous strain analysis by one observer (O) and analytic solution (curved line). In a–d, numbers on x axis are millimeters; R = radial position. (a) Most positive eigenvalue. (b) Most negative eigenvalue. (c) Principal angle. (d) Rotation angle.

The existence of simple analytic solutions to the finite deformation problems enabled comparison of HS triangles and higher-order finite elements with the expected strain field under both noiseless and noisy conditions. The noiseless HS error (Fig 6, open circles) is due to the assumption of constant strain within each triangle. The error increases with the gradient of strain toward the inner cylinder, and it appears to be random because triangles of different orientation cover different lengths in the radial direction (the direction of greatest strain variation). In previous studies, Douglas et al (13) and McCulloch and Omens (15) quantified the error due to the homogeneous strain

approximation by simulating the approximate physiologic deformation of the middle ventricular free wall. These studies did not quantify the effect of noise on the calculated strain; however, McCulloch and Omens (15) noted that a nonhomogeneous finite-element analysis of implanted bead data produced less variation in the time series of strain throughout the cycle.

Some approximations were made in the derivation of the analytic solution. First, the deformation was assumed to be one dimensional: $\theta(R)$ for axial shear and $z(R)$ for azimuthal shear. In general, small radial displacements are expected in both cases near the free edges of the material because of

Table 4
Average Errors in Nonhomogeneous Strain Calculation in Axial Shear

Comparison of Values	Average Error				
	λ_1	λ_2	β^*	α^*	ΔA
O/O	0.063	0.040	5.59	2.09	0.075
O/A	0.075	0.031	5.31	2.10	0.062
SSS/A	0.050	0.012	2.32	0.89	0.036
M/A	0.010	0.003	0.15	0.29	0.032
Percentage of analytic solution					
O/A	14	8	8	24	6
M/A	5	4	3	10	3

Note.—O/O = observer/observer, O/A = observers/analytic model, SSA/A = single-shot SPAMM image/analytic model, M/A = modeled displacement (noiseless)/analytic model, λ_1 and λ_2 = principal strains, β = principal angle, α = rotation angle, ΔA = change in area.

* Degrees, except for percentage of analytic solution.

Table 5
Average Errors in Nonhomogeneous Strain Calculation in Azimuthal Shear

Comparison of Values	Average Error				
	λ_1	λ_2	β^*	α^*	ΔA
O/O	0.023	0.021	0.95	2.95	0.035
O/A	0.044	0.016	3.06	0.99	0.028
M/A	0.007	0.002	0.13	0.23	0.001
Percentage of analytic solution					
O/A	18	10	6	9	3
M/A	2	1	0	2	0

Note.—O/O = observer/observer, O/A = observers/analytic model, M/A = modeled displacement (noiseless)/analytic model, λ_1 and λ_2 = principal strains, β = principal angle, α = rotation angle, ΔA = change in area.

* Degrees, except for percentage of analytic solution.

the Kelvin effect (26). In the case of azimuthal shear, the solution became increasingly inaccurate toward the free edges (Fig 2d); hence, only the inner two-thirds of the image was used. For axial shear, no appreciable difference was found in the displacement field between images at the free edge ($Z = 2.5$ mm) and central ($Z = 17.5$ mm) circumferential planes. The angular displacement of stripes painted on the surface of the gel also agreed with that of tags in the central plane.

Second, the gel material was assumed to obey a Mooney-Rivlin constitutive law. This is the simplest hyperelastic material law that accurately models the displacement fields in our simple, quasistatic equilibrium experiments. The derived displacements are also independent of the material constants (stiffness or bulk and shear modulus). A more complicated material law may be required to model other experiments performed over different durations (eg, experiments that include viscoelastic, stress-softening, or creep effects).

Third, inertial effects caused by gravity or sudden accelerations were

assumed to be small compared with the imposed deformations and image resolution. Only slight deformation under gravity was observed, and no transients caused by hitting the stops were noticed.

Because simple shear in one coordinate system is equivalent to biaxial stretch in another, a wide range of deformations are represented by this phantom. However, the deformations are not intended to model those that occur in the beating heart. The shear strains are many times higher and the strain field is considerably less homogeneous than those in the normal human heart (5). In previous simulations of contraction, the greatest error occurred in transmural shear strains (13,15). Thus, our shear deformation modes represent worst-case situations, especially as the strain gradients become very high near the inner cylinder. The errors obtained with the phantom are therefore expected to be higher than those in the heart. However, small errors in tag intersection location (eg, 0.42 mm for axial shear) can cause large errors in the principal strains (33% for λ_1). For clinical use, this noise can be reduced by averag-

ing a number of triangles in a region in which the strain does not vary greatly, because the estimates are unbiased. Alternatively, a nonhomogeneous approach reduces the noise by smoothing the displacement field. In either case, the biologic variation is expected to exceed the errors of the method (eg, in a previous study [12], the variation in maximum principal strain between four dogs was approximately 33%).

A phantom that mimics the physiologic strain field of the heart could be used to determine the optimum tag spacing and order of the finite-element model for a particular image resolution. Analytic solutions for the strain field do not exist in general; however, if a realistic material law is assumed, it is possible to obtain accurate solutions with the finite-element method (27). Deformable phantoms of the type described herein could also be used to validate three-dimensional reconstructions of deformation (28–30) and quantify the effect of image S/N, respiration artifacts, and variable RR interval on the calculated deformations. In conclusion, our results demonstrate that MR tagging provides an accurate estimate of the displacement field within a deformed body. Unbiased estimates of the strain field can be easily obtained; however, greater accuracy can be achieved with nonhomogeneous finite-element approximations than with homogeneous strain triangles.

APPENDIX

Analytic solutions for simple deformations of a cylinder are discussed by Adkins (22), Spencer (23), and Green and Zerna (21). In our study, the deformations are described by the following:

$$r = R; \quad \theta = \omega(R) + \Theta; \quad z = Z \quad (A1)$$

for axial shear and

$$r = R; \quad \theta = \Theta; \quad z = \gamma(R) + Z \quad (A2)$$

for azimuthal shear, where R , Θ , and Z are coordinates of a material point in the undeformed state and r , θ , and z are the corresponding coordinates in the deformed state. Here, ω and γ are the angular and longitudinal displacements (functions of R only) caused by the applied loads. In reality, because of the large deformations undergone, small displacements normal to the applied loads occur in each case unless tractions are applied to the free ends. This is called the Kelvin effect (26) and occurs in all incompressible isotropic hyperelastic materials. However, these displacements are small and must be zero in the central Z plane of the phantom because of the symmetry of the applied loads and the isotropic nature of the material.

Axial Shear

In this case, the deformation gradient tensor (F) (in cylindrical polar coordinates) is as follows (23):

$$F = \begin{bmatrix} 1 & 0 & 0 \\ R\omega' & 1 & 0 \\ 0 & 0 & 1 \end{bmatrix}, \quad (A3)$$

where ω' is the derivative of ω with regard to R . The Cauchy stress tensor (T) for an isotropic incompressible material is as follows (23):

$$T = -pI + 2 \left(\frac{\partial W}{\partial I_1} + I_1 \frac{\partial W}{\partial I_2} \right) B - 2 \frac{\partial W}{\partial I_2} B^2, \quad (A4)$$

where p is hydrostatic pressure and I_1 and I_2 are the first and second invariants of $B = FF^T$. The equations of equilibrium (neglecting body forces and inertial effects) are as follows: $\text{div } T = 0$. For a Mooney-Rivlin (rubberlike) material, the constitutive law is expressed by the strain energy function:

$$W = C_1(I_1 - 3) + C_2(I_2 - 3), \quad (A5)$$

where C_1 and C_2 are material constants. Examination of the equilibrium equation for the radial-circumferential component of the stress tensor, $t_{r\theta}$, yields the following:

$$t_{r\theta} = KR^{-2}, \quad (A6)$$

where K is a constant of integration. Substitution of A4 and A5 yields the following:

$$\omega = \frac{-K}{4R^2(C_1 + C_2)} + L, \quad (A7)$$

where L is another constant of integration. Substitution of the boundary conditions $\omega(R_1) = \omega_1$ and $\omega(R_2) = 0$ produces the following:

$$\omega(R) = \omega_1 \frac{(R_2^{-2} - R^{-2})}{(R_2^{-2} - R_1^{-2})}, \quad (A8)$$

where ω_1 is the angle of rotation of the inner cylinder. Note that the displacement (and hence the deformation) is independent of the material constants C_1 and C_2 (ie, the deformation is unchanged by the stiffness of the gel [or ratio of part A to part B]).

Azimuthal Shear

This case is similar to that in "Axial Shear," except the deformation gradient tensor is now the following:

$$F = \begin{bmatrix} 1 & 0 & 0 \\ 0 & 1 & 0 \\ \gamma' & 0 & 1 \end{bmatrix}, \quad (A9)$$

where γ' is the derivative of γ and the appropriate equation governing equilibrium is as follows:

$$t_{rz} = AR^{-1}, \quad (A10)$$

which produces the following:

$$\gamma(R) = \frac{\gamma_1[\ln(R) - \ln(R_2)]}{[\ln(R_1) - \ln(R_2)]}, \quad (A11)$$

where γ_1 is the longitudinal translation of the inner cylinder relative to the outer cylinder and $\ln =$ natural logarithm. Thus, deformation in this mode is also independent of material stiffness. ■

Acknowledgments: David A. Rahdert, MS, contributed many ideas on phantom design and motion control. Chandra M. Sehgal, PhD, digitized the video images. Daniel Bloomgarden, MSE, Cheng-Ning Chang, MSE, Dara Kraitchman, MSE, and Zahi A. Fayad, MSE, helped with image analysis.

References

- Herman MV, Heinle RA, Klein MD. Localized disorders in myocardial contraction: asynergy and its role in congestive heart failure. *N Engl J Med* 1967; 277:222-232.
- Yin FCP. Ventricular wall stress. *Circ Res* 1981; 49:829-842.
- Zerhouni EA, Parish DM, Rogers WJ, Yang A, Shapiro EP. Human heart: tagging with MR imaging—a method for noninvasive assessment of myocardial motion. *Radiology* 1988; 169:59-63.
- Rogers W, Shapiro E, Weiss J, et al. Quantification of and correction for left ventricular systolic long-axis shortening by magnetic resonance tissue tagging and slice isolation. *Circulation* 1991; 84:721-731.
- Axel L, Gonçalves R, Bloomgarden D. Regional heart wall motion: two-dimensional analysis and functional imaging with MR imaging. *Radiology* 1992; 183:745-750.
- Buchalter MB, Weiss JL, Rogers WL, et al. Noninvasive quantification of left ventricular rotational deformation in normal humans using magnetic resonance imaging myocardial tagging. *Circulation* 1990; 81:1236-1244.
- Lima J, Ferrari V, Palmon L. Myocardial rigid body translation and rotation by magnetic resonance tissue tagging before and after infarction (abstr). *Circulation* 1991; 84(suppl 2):201.
- Clark N, Reichel N, Bergy P, et al. Circumferential myocardial shortening in the normal human left ventricle. *Circulation* 1991; 84:67-74.
- Axel L, Dougherty L. Heart wall motion: improved method of spatial modulation of magnetization for MR imaging. *Radiology* 1989; 172:349-350.
- Walley KR, Grover M, Raff GL, Bengt JW, Hannaford B, Glantz SA. Left ventricular dynamic geometry in the intact and open chest dog. *Circ Res* 1982; 50:573-589.
- Villarreal FL, Waldman LK, Lew WYW. Technique for measuring regional two-dimensional finite strains in canine left ventricle. *Circ Res* 1988; 62:711-721.
- Waldman LK, Fung YC, Covell JW. Transmural myocardial deformation in the canine left ventricle: normal in vivo three-dimensional finite strains. *Circ Res* 1985; 57:152-163.
- Douglas AS, Hunter WC, Wiseman MD. Inhomogeneous deformation as a source of error in strain measurements derived from implanted markers in the canine left ventricle. *J Biomech* 1990; 23:331-341.
- Young AA, Hunter PJ, Smaill BH. Estimation of epicardial strain using the motions of coronary bifurcations in biplane cineangiography. *IEEE Trans Biomed Eng* 1992; 39:526-531.
- McCulloch AD, Omens JH. Non-homogeneous analysis of three-dimensional transmural finite deformations in canine ventricular myocardium. *J Biomech* 1991; 24:539-548.
- Ingels NB, Daughters GT, Stinson ED, Alderman EL. Evaluation of methods for quantitating left ventricular segmental wall motion in man using myocardial markers as a standard. *Circulation* 1980; 61:966-972.
- Yeon S, Reichel N, Palmon L, et al. Myocardial segment shortening in canine myocardial infarction using spatial modulation of magnetization and sonomicrometry (abstr). In: Book of abstracts: Society of Magnetic Resonance in Medicine 1990. Berkeley, Calif: Society of Magnetic Resonance in Medicine, 1990; 270.
- McVeigh E, Zerhouni EA. Noninvasive measurement of transmural gradients in myocardial strain with MR imaging. *Radiology* 1991; 180:677-683.
- Goldstein DC, Kundel HL, Daube-Witherspoon ME, Thibault LE, Goldstein EJ. A silicone gel phantom suitable for multimodality imaging. *Invest Radiol* 1987; 22:153-157.
- Margulies S, Thibault L, Gennarelli T. Physical model simulations of brain injury in the primate. *J Biomech* 1990; 23:823-836.
- Green AE, Zerna W. *Theoretical elasticity*. London, England: Oxford University, 1968; 99.
- Adkins JE. Some general results in the theory of large elastic deformations. *Proc Royal Soc A* 1955; 231:75-90.
- Spencer AJM. *Continuum mechanics*. London, England: Longman, 1980; 153-163.
- Haase A. Snapshot FLASH MRI: applications to T1, T2, and chemical-shift imaging. *Magn Reson Med* 1990; 13:77-89.
- Niitsu M, Campeau NG, Holsinger-Bampton AE, Riederer SJ, Ehman RL. Tracking motion with tagged rapid gradient-echo magnetization-prepared MR imaging. *JMRI* 1992; 2:155-163.
- Adkin RJ, Fox N. *An introduction to the theory of elasticity*. New York, NY: Longman, 1980; 56-122.
- Zienkiewicz O. *The finite element method*. London, England: McGraw-Hill, 1977.
- Pelc NJ, Herfkens RJ, Shimakawa A, Enzmann DR. Phase contrast cine magnetic resonance imaging. *Magn Reson Q* 1991; 7:229-254.
- Moore CC, O'Dell WC, McVeigh ER, Zerhouni EA. Calculation of three-dimensional left ventricular strains from biplanar tagged MR images. *JMRI* 1992; 2:165-175.
- Young AA, Axel L. Three-dimensional motion and deformation of the heart wall: estimation with spatial modulation of magnetization—a model-based approach. *Radiology* 1992; 185:241-247.